Experimental and Numerical Studies of Ethanol Decomposition Reactions

Juan Li,* Andrei Kazakov, and Frederick L. Dryer

Department of Mechanical & Aerospace Engineering, Princeton University, Princeton, New Jersey 08544

Received: May 7, 2004; In Final Form: July 15, 2004

Ethanol pyrolysis experiments at 1.7−3.0 atm and 1045−1080 K were performed in the presence of radical trappers using a variable pressure flow reactor. Stable species time histories were determined using continuous sampling, on-line Fourier transform infrared spectrometry, and off-line gas chromatography. The rate constant k_1 of the molecular decomposition reaction, $C_2H_5OH \rightarrow C_2H_4 + H_2O$ (R1), was determined experimentally. The obtained result agrees very well with extrapolation of the recent shock-tube data of Herzler et al.[1] The multichannel unimolecular decomposition of ethanol was also investigated theoretically on the basis of RRKM/master equation calculations. The effects of the hindered rotations in C_2H_5OH and quantum tunneling on the molecular decomposition reaction were taken into account. The reaction R1 was found to be strongly dependent on temperature and the dominant channel over the range of temperatures 300−2500 K at 1 atm. The calculated k_1 is in excellent agreement with the recent theoretical work of Tsang[2] as well as with the experimental measurements of Herzler et al.[1] and the present data. The influence of tunneling on the shape of the falloff is discussed. In addition, the RRKM/master equation results were fit to modified Arrhenius expressions to facilitate chemical kinetic modeling applications of the results.

Introduction

Ethanol (C_2H_5OH) is a very important energy carrier that can be produced from renewable energy resources. It can be used as a fuel extender, octane enhancer, and oxygen additive in, or as an alternative to, neat fuel to replace reformulated gasoline. Ethanol also has potential as a hydrogen carrier for fuel-cell applications. The 1990 Clean Air Act Amendments[3] presently require the addition of oxygenates to reformulated gasoline, with seasonal adjustments, on the premise that oxygen content decreases automotive emissions, particularly smog-generation participants and CO. Ethanol is favored to replace methyl tertiary butyl ether (MTBE), another widely used oxygenate additive that has become unpopular on the basis of groundwater contamination and human health effects. Although most ethanol is currently generated by fermentation (grain alcohol), recent developments suggest that ethanol fuel can be derived more efficiently from other types of biomass, thus offering the potential to reduce dependence on fossil-fuel energy resources.

The chemical kinetics of ethanol related to combustion has been extensively studied in many previous works, with the most recent detailed modeling studies being those of Marinov.[4] His work emphasized the high sensitivity of experimentally measured ignition delay during shock-induced decomposition of rich ethanol mixtures to the rate constants of ethanol decomposition reactions. Moreover, his analyses showed that high-temperature ethanol oxidation is strongly sensitive to the falloff kinetics of the ethanol decomposition process and to the branching ratio assignments among the ethanol abstraction reactions. Unfortunately, there were few ethanol pyrolysis data available for comparison at the time of this modeling work. Although our recent ethanol pyrolysis experiments[5] using the same variable pressure flow reactor (VPFR) employed here showed that H_2O and C_2H_4 are the major products of ethanol thermal decomposition, we found that Marinov's model underestimated their production rate as well as the overall ethanol consumption rate. We also confirmed that ethanol pyrolysis is very sensitive to the decomposition reactions

$$C_2H_5OH \rightarrow C_2H_4 + H_2O \qquad \text{(R1)}$$

$$C_2H_5OH \rightarrow CH_3 + CH_2OH \qquad \text{(R2)}$$

as well as to hydrogen abstraction reactions with CH_3 radicals, which primarily come from reaction R2. Because the decomposition and abstraction pathways are coupled during both pyrolysis and oxidation, an accurate description of the unimolecular decomposition process over a wide range of conditions is needed to further understand the contributions of the abstraction reactions in comprehensive kinetic models for describing ethanol combustion.

Recently, Tsang[2] conducted a theoretical study of the ethanol decomposition reactions. His predictions for the rate coefficient of reaction R1 agree within 30% of those of Marinov at our experimental conditions.[5] However, Tsang pointed out that Marinov's analyses of the other dissociation reactions were flawed, because each was treated individually in his calculations. As a consequence, the competition among the different channels was not considered properly, and the derived rate coefficients for the dissociation reactions including that of reaction R2 were grossly overestimated. Additionally, Park et al.[6] have conducted low-temperature static-reactor pyrolysis experiments and high-temperature shock-tube experiments to determine the rate constants of ethanol decomposition reactions. Park et al. also performed a theoretical study of ethanol decomposition reactions.[7] Their prediction for the rate coefficient of reaction R1 is approximately one-third of Tsang's[2] at 1100 K and 1 atm (i.e., at conditions attainable using flow reactors).

In the present study, we conducted ethanol pyrolysis experiments in a variable pressure flow reactor in the presence of either toluene or 1,3,5-trimethylbenzene as a radical trapper to

* Corresponding author. E-mail: juanli@princeton.edu.

10.1021/jp0480302 CCC: $27.50
Published on Web 08/31/2004

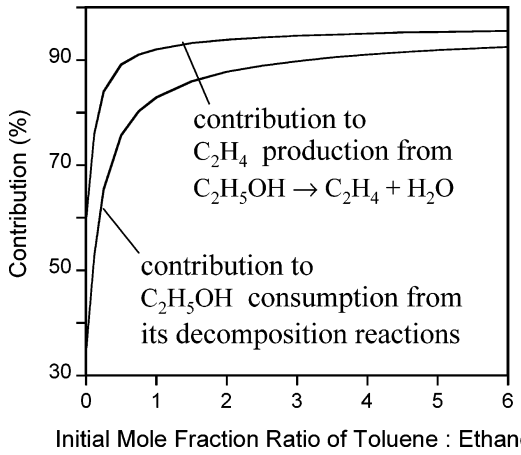

Figure 1. Integrated contributions of specified reactions to ethanol consumption and C_2H_4 yield in pyrolysis as a function of the toluene/ethanol mole fraction in the initial mixture. Model: ethanol (Marinov[4]) and toluene (Emdee et al.[8]). Initial conditions: $T = 1050$ K, $P = 3$ atm, $C_2H_5OH = 0.15\%$ with corresponding toluene and balance N_2.

determine the rate constant of reaction R1. The multichannel thermal decomposition of ethanol was also studied theoretically by using the RRKM/master equation approach. Both the experimental data and the theoretical results are compared with the prior literature.

Experiments with Radical Trappers

The ethanol decomposition reactions via either C−C or C−O bond dissociation generate radicals, including CH_3. These radicals can further react with the fuel by abstracting H-atoms, producing intermediates leading to C_2H_4, CH_4, and so on. Therefore, both the fuel consumption and the yield of major intermediates (such as C_2H_4) come from multiple sources involving both decomposition and abstraction reactions. To reduce the contribution of abstraction reactions, toluene or 1,3,5-trimethylbezene is used as a radical trapper in ethanol pyrolysis experiments. Each of these species reacts more rapidly than ethanol with radicals produced from ethanol dissociation to form species that do not regenerate reactive radical species on similar time scales. For example, toluene undergoes the following reactions with radicals:

$$H + C_6H_5CH_3 \rightarrow CH_3 + C_6H_6$$

$$X + C_6H_5CH_3 \rightarrow XH + C_6H_5CH_2$$

$$X + C_6H_5CH_2 \rightarrow C_6H_5CH_2X$$

$$(X = CH_3, OH, O, H)$$

Radical trappers compete so strongly with ethanol for the radicals formed by ethanol decomposition that few react with ethanol itself and contribute to ethanol consumption and C_2H_4 production. In other words, in the presence of radical trappers, ethanol will be destroyed primarily by its decomposition reactions, and C_2H_4 will be generated primarily from the molecular reaction R1 alone. The influence of toluene as a radical trapper on ethanol pyrolysis is illustrated in Figure 1. The figure shows the integrated contribution (after 80% of the initial ethanol concentration is consumed) to ethanol destruction from all of its decomposition reactions and the contribution of reaction R1 alone to the yield of C_2H_4 as a function of the initial mole fraction ratio of toluene to ethanol at 1050 K and 3 atm. The results were calculated using the ethanol mechanism of Marinov[4] combined with the toluene mechanism of Emdee et al.[8] The presence of toluene at adequate concentrations relative to ethanol emphasizes the role of decomposition reactions, especially reaction R1, in both the fuel disappearance and the ethylene yield. For example, without toluene addition, approximately 60% of C_2H_4 comes from reaction R1, while 92% results from this channel when toluene is present at the same initial mole fraction as ethanol. Thus, by measuring the concentrations of stable species in pyrolysis seeded with toluene, the rate constant of the molecular reaction R1 can be determined experimentally.

On the basis of these results, ethanol pyrolysis experiments with the addition of toluene were performed in a VPFR. Herzler et al.[1] used a similar technique in their shock-tube pyrolysis studies, with 1,3,5-trimethylbenzene as the radical trapping species. We also performed flow reactor studies with this radical trapper.

The flow reactor is a continuous flow device, where the reactants are highly diluted in an inert carrier gas, and the total flow rate is very large. The diluted reactions are sufficiently slow such that the reaction zone itself occurs over a large physical distance in the reacting flow. Thus, the flow reactor provides an experimental means to directly measure the chemical kinetics by determining the species−distance profiles and interpreting them as species time history information. A schematic diagram of the flow reactor is shown in Figure 2. The entire reactor is enclosed in a carbon-steel pressure vessel rated for operation from full vacuum to 30-atm pressure, permitting experiments to be carried out over a wide range of ambient pressures. The reactor is maintained at pressures above atmospheric pressure through control of a backpressure valve at the reactor exit.

Carrier gas (N_2 in this study) is heated by a pair of electrical resistance heaters and directed into the 10.16-cm diameter quartz reactor duct in which the reaction zone is to be stabilized. The flow enters the tube and then passes around an 8.9-cm baffle plate and radially inward into a 0.64-cm gap which serves as the entrance to a silica foam diffuser (Figure 3). The liquid fuel (mixed with radical trappers in this study) is vaporized as an aerosol suspended in heated nitrogen inside a 300-cm^3 stainless-steel cylinder maintained at temperatures above the saturation point of the local mixture fraction. The nitrogen/vapor mixture is delivered through the center passage of a fuel injector probe to the location of the inward-directed carrier flow and exits the fuel injector through a large number of orifices as opposed jets. Additional N_2 is introduced via an annular passage in the fuel injector probe to prevent excessive heating of the fuel vapor/nitrogen flow inside the fuel injector probe. The buffering flow exits the fuel injector probe through a second set of injector orifices at the mixing location of carrier gas and fuel vapor/nitrogen flows.

After fuel vapor injection and mixing, the reacting mixture then flows through the 5° half-angle diffuser into a constant area test section. At different distances from the injector location, a hot-water-cooled, stainless-steel sampling probe is positioned on the flow centerline and convectively quenches and continuously extracts a small portion of the reacting flow. The gas-extracted and -quenched sample stream flows through heated Teflon lines and a multiport sampling valve. The (heated) multiport sampling valve can be used to trap and store up to 16 individual volumes of sample flow for subsequent off-line analyses using a Hewlett-Packard 6890 gas chromatograph equipped with a hydrogenation catalyst and flame ionization detection. This ex situ analysis allows for the identification and

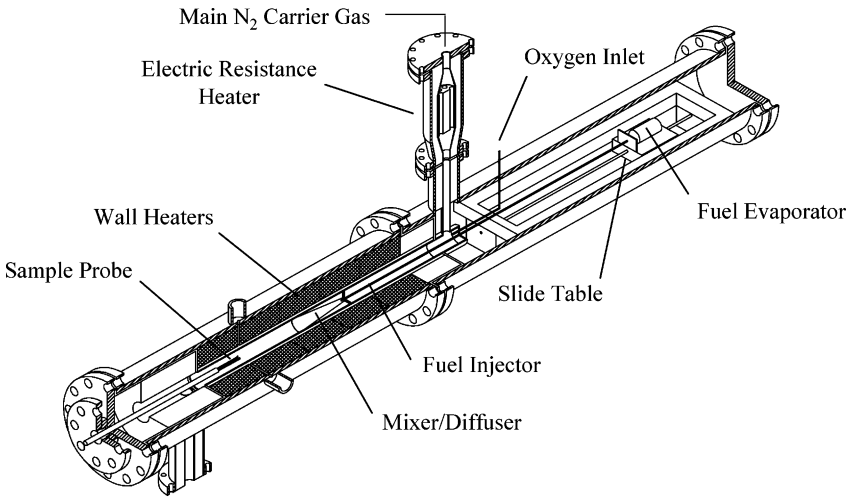

Figure 2. Schematic diagram of the variable pressure flow reactor (VPFR).

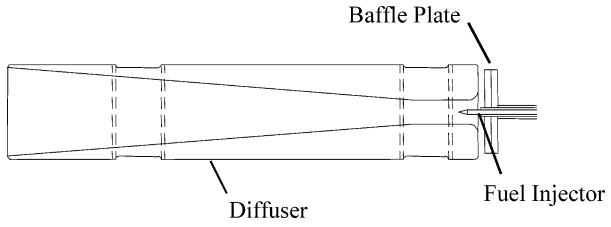

Figure 3. Schematic diagram of the fuel injector/mixer/diffuser assembly.

quantification of the stable species related to radical trappers, such as toluene, benzene, ethylbenzene, and 1,3,5-trimethylbenzene. The sampled flow directed through the multiport valve is then directed through the following on-line analyzers: (1) a Nicolet Magna IR 560 Fourier transform infrared (FTIR) spectrometer for measurement of the majority of the stable species of interest (C_2H_5OH, H_2O, C_2H_4, CH_4, CH_3CHO, CH_2O, and so on), (2) a pair of Horiba model PIR-2000 nondispersive infrared analyzers to measure CO and CO_2 concentrations, and (3) a DELTA F Type A Plus electrochemical analyzer to monitor the initial trace O_2 concentrations present in the nitrogen carrier supply. The measurement uncertainties for the data reported here are as follows: CO = ±2%, C_2H_5OH = ±2%, H_2O = ±6%, C_2H_4 = ±2%, CH_4 = ±3%, and CH_3CHO = ±4% of the reading. The temperature of the reacting mixture is measured locally at the point of sampling using a silica-coated type-R thermocouple accurate to ±3 K.[9]

The distance between the point of fuel injection and the sampling position is varied by moving the injector with attached mixer/diffuser assembly relative to the fixed sampling location by means of a slide table driven by a computer-controlled stepper motor. Mean velocity measurements along the centerline of the reactor are used to correlate distance with residence time. Experimental conditions are chosen to produce reaction zones in which 1 cm of reaction distance corresponds to a reaction time between 10^{-4} and 10^{-2} s. In the present study, data points were taken at 5-cm intervals.

The high degree of dilution of the C_2H_5OH/radical trappers/N_2 mixture used in this study ensures that the maximum chemical enthalpy change due to reaction is small. Five individually controlled electrical resistance heaters maintain the local wall temperature of the quartz reactor duct at the initial gas temperature, establishing a nearly adiabatic condition at the reactor walls. As a result of these two conditions, the local gas

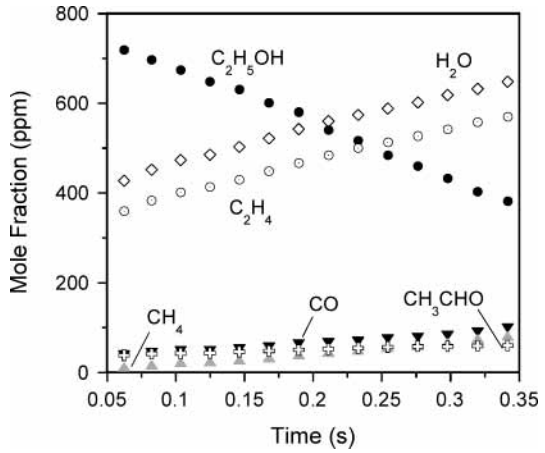

Figure 4. Profiles of stable species measured in the VPFR test section in an ethanol pyrolysis experiment. Initial conditions: T = 1050 K, P = 3.0 atm, C_2H_5OH = 0.12%, $C_6H_5CH_3$ = 0.12% with balance N_2 (trace O_2 = 35 ppm).

temperature variation from the initial reaction temperature is due solely to chemical enthalpy changes.

A series of pyrolysis experiments were conducted at 1.7−3.0 atm and 1045−1080 K with ethanol and radical trappers of equal initial concentrations. Figure 4 shows the mole fraction profiles of stable species related to ethanol pyrolysis in the VPFR test section for an experiment at 1050 K and 3 atm. Temperature is not shown here because, for pyrolysis, it remains nearly constant (within approximately 4 K). As shown in Figure 4, H_2O and C_2H_4 are the major products of ethanol thermal decomposition. In the present work, measured C_2H_5OH and C_2H_4 concentrations were used to estimate the rate constant of reaction R1, k_1, according to the standard rate equation:

$$\frac{d[C_2H_4]}{dt} = k_1 \cdot [C_2H_5OH] \qquad \text{(E1)}$$

where [X] is the concentration of species X, and t is the reaction time. The experimentally determined rate constant k_1 is presented in Figure 5. The excellent agreement between the experimental data using different kinds of radical trappers further supports the present experimental methodology. Experimental uncertainties are also reported in Figure 5. The uncertainty in the temperature measurements, shown horizontally, is less than ±0.4%. At each fixed temperature, the total uncertainty in the determined rate, shown vertically, is approximately ±15%,

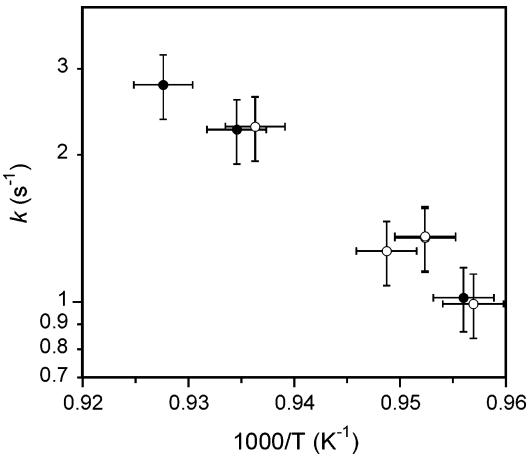

Figure 5. Rate constant of the reaction $C_2H_5OH \rightarrow C_2H_4 + H_2O$ determined in the present flow reactor experiments. Open symbols represent results by using toluene as a radical trapper; closed symbols represent results by using 1,3,5-trimethylbenzene as a radical trapper.

including those from the experimental measurements and the methodology itself. The experimental values of k_1 obtained here are in very good agreement with extrapolation of the shock-tube pyrolysis measurements of Herzler et al.[1] taken at higher temperatures (see Figure 8).

Theoretial Calculation Of Rate Constants

The multichannel unimolecular decomposition reactions of ethanol were also investigated theoretically on the basis of the RRKM/master equation approach. In addition to reactions R1 and R2, we initially also considered reactions R3 and R4:

$$C_2H_5OH \rightarrow C_2H_5 + OH \qquad (R3)$$

$$C_2H_5OH \rightarrow CH_3CH + H_2O \qquad (R4)$$

The rate constants k_3 and k_4 were estimated to be much lower than k_1 and k_2 at our conditions, and they become competitive at very high temperatures (above 2500 K). For example, at 1 atm and 1100 K, k_3 and k_4 are lower than k_1 by 3−4 orders of magnitude and lower than k_2 by 1−2 orders of magnitude. The ab initio results of Park et al.[7] also predict that reactions R1 and R2 are the dominant channels over the entire range of conditions of practical interest. As a result, only reactions R1 and R2 were considered in further detail in the present study.

Equilibrium geometries of the reactants, transition states, and products were optimized by second-order Moller−Plesset perturbation theory (MP2) with the 6-311G(d,p) basis set. Vibrational frequencies calculated by the same method were scaled by a factor of 0.9748[10] and employed for zero-point energy (ZPE) correction and rate constant calculation. Electronic energies of the species were evaluated at the G2 level of theory.[11] We also investigated the geometries by the hybrid density functional B3LYP method[12] with the 6-31G(d) basis set and energies at the G3B3 level of theory.[13] The *Gaussian 98* package[14] was used for all molecular orbital calculations. The moments of inertia and scaled vibrational frequencies of all species used in the present RRKM calculation are summarized in Table 1. A schematic diagram of the potential energy surface for the ethanol decomposition process is shown in Figure 6. Table 2 contains the energy barriers (including a ZPE correction at 0 K) calculated by different theoretical methods, as well as available experimental results. Clearly, all theoretical results are in reasonable agreement with each other. In particular, the energy barrier for the H_2O elimination reaction R1 obtained in the present study by both methods matches very well with the recent G2M calculations of Park et al.[7]

Special consideration was given to two hindered rotations present in C_2H_5OH, the CH_3- and $OH-$ internal rotors. The calculated torsional potential of the CH_3- internal rotor has a symmetry number of 3, while the $OH-$ internal rotor is nonsymmetric. Detailed information can be found in Appendix A.

Rate constants were computed by using the *ChemRate* package (version 1.19)[20] and an in-house computer code. For both codes, the molecular parameters (reaction barriers, moments of inertia, and vibrational frequencies) are required as input for the sum and density of states computations, followed by the microscopic rate constant $k(E)$ calculation based on the RRKM theory.[21] With the input information for the collision model, rate constants are calculated after solving the master equations.[21] The in-house computer program was specifically designed for computational efficiency (thus allowing extensive parametric studies without sacrificing the accuracy) and incorporates features that are not available in the *ChemRate* package. These features include arbitrary energy and temperature dependence of $\langle \Delta E_{down} \rangle$ (see text to follow), a more rigorous treatment of hindered rotations described in Appendix B, and evaluation of microscopic rate coefficients for loose transition states from the prescribed high-pressure-limit rate constant.

The molecular parameters were based on MP2(FC)/6-311G-(d,p) calculations shown in Table 1. In the calculations, the energies of stable compounds with respect to C_2H_5OH were adjusted to their experimental values shown in Table 2. The scaling factor for the two lowest vibrational frequencies of the tight transition state $C_2H_4-H_2O$ and the barrier of reaction R1 were optimized to achieve the best agreement with the present experimental data shown in Figure 5 and the data of Herzler et al.[1] The optimization resulted in a barrier height of 64.3 kcal/mol and scaling factor of 0.58. Although the adjustment of the barrier by approximately 2 kcal/mol is very typical and well within the accuracy of quantum chemical calculations, the scaling factor for the lowest frequencies appears to be inordinately low. Attempts to use larger basis sets for transition-state optimization conducted in this study did not resolve this controversy; more sophisticated calculations may be needed in the future.

The microscopic rate coefficient for the transition state CH_3-CH_2OH of the C−C bond fission reaction R2 was estimated using a prescribed high-pressure-limit rate constant. The procedure used here is based on the assumptions of the Gorin model for the loose transition state.[21] The vibrational frequencies for this transition state were assigned by using those of the two fragments, CH_3 and CH_2OH, and its standard heat of formation was taken as the sum of the heats of the two fragments. As can be shown,[21] the quantitative information regarding the remaining rotational degrees of freedom (i.e., rotational constants, symmetry, simple steric hindrance) enters the density of states and, therefore, the microscopic rate coefficient in the form of constant multipliers. Thus, one can simply evaluate the microscopic rate coefficient using arbitrarily assigned rotational constants and then scale it to match the prescribed value of k_∞ at a given temperature. Obviously, the resulting scaling factor will also be a function of temperature. The prescribed value of $k_{2\infty}$ was derived from the equilibrium constant and $k_{-2\infty}$, the high-pressure-limit rate constant of the reverse (recombination) reaction of R2. In this study, $k_{-2\infty}$ was fixed at 1.2×10^{13} cm^3 mol^{-1} s^{-1}. This is a suggested value from the literature[22] and is

TABLE 1: Moments of Inertia (I_A, I_B, I_C) and Vibrational Frequencies of Species Involved in the Ethanol Decomposition Reactions

species	method	I_A, I_B, I_C[a]	frequencies[b] (degeneracy)
C_2H_5OH	MP2(FC)/6-311G(d,p)	14.5, 53.5, 61.6	230[c], 282[c], 412, 815, 903, 1041, 1112, 1174, 1268, 1294, 1382, 1451, 1463, 1487, 1518, 2960, 3002, 3008, 3099, 3105, 3813
	B3LYB/6-31G(d,p)	14.5, 54.0, 62.1	240, 288, 401, 797, 875, 1001, 1079, 1147, 1240, 1258, 1370, 1422, 1453, 1470, 1499, 2863, 2886, 2936, 3004, 3009, 3601
C_2H_4	MP2(FC)/6-311G(d,p)	3.46, 16.9, 20.3	807, 891, 946, 1046, 1205, 1349, 1444, 1638, 3098, 3115, 3185, 3211
	B3LYB/6-31G(d,p)	3.43, 16.8, 20.3	801, 918, 937, 1027, 1198, 1340, 1435, 1651, 3026, 3041, 3093, 3118
H_2O	MP2(FC)/6-311G(d,p)	0.64, 1.12, 1.77	1626, 3806, 3911
	B3LYB/6-31G(d,p)	0.64, 1.17, 1.81	1645, 3578, 3695
$C_2H_4-H_2O$ (transition state)	MP2(FC)/6-311G(d,p)	18.1, 53.5, 63.3	1926*i*, 205, 293, 577, 615, 757, 811, 832, 1084, 1150, 1220, 1232, 1429, 1439, 1504, 1658, 3075, 3101, 3168, 3199, 3680
	B3LYB/6-31G(d,p)	19.0, 55.5, 66.3	1928*i*, 366, 422, 542, 608, 710, 800, 813, 993, 1083, 1195, 1197, 1402, 1425, 1490, 1553, 3021, 3031, 3095, 3122, 3523
CH_3	MP2(FC)/6-311G(d,p)	1.76, 1.76, 3.52	407, 1411(2), 3094, 3282(2)
	B3LYB/6-31G(d,p)	1.77, 1.77, 3.55	435, 1374(2), 3018, 3185(2)
CH_2OH	MP2(FC)/6-311G(d,p)	2.59, 16.8, 19.4	454, 715, 1062, 1202, 1363, 1490, 3093, 3240, 3825
	B3LYB/6-31G(d,p)	2.66, 17.0, 19.4	433, 653, 1029, 1170, 1326, 1447, 3001, 3139, 3611

[a] Unit = amu·Å^2. [b] Unit = cm^{-1}. Frequencies obtained at MP2(FC)/6-311G(d,p) level of theory are scaled by a factor of 0.9748, except that the lowest two frequencies of $C_2H_4-H_2O$ are scaled by a factor of 0.58 to match the experimental results. Frequencies at B3LYB/6-31G(d,p) level are scaled by a factor of 0.96. [c] These two vibration modes are replaced by two hindered rotors of C_2H_5OH (see text).

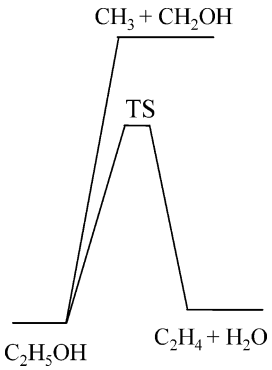

Figure 6. Schematic diagram of the potential energy surface of the ethanol decomposition process.

TABLE 2: Energy (Including ZPE Correction) Relative to C_2H_5OH for Ethanol Decomposition at 0 K[a]

methods	$C_2H_4-H_2O$ (transition state)	$C_2H_4 + H_2O$	$CH_3 + CH_2OH$
Setser et al.[15] MP2(FU)/6-311G(d,p) with MP4SDQ(FC)/6-311+G(2d,2p)	67.1	9.4	82.5
Park et al.[7] G2M//B3LYP/6-311G(d,p)	66.6	6.5	87.5
this study G2//MP2(FC)/6-311G(d,p)	66.8	9.9	86.9
this study G3B3//B3LYP/6-31G(d)	66.6	9.4	84.3
experimental data	64.3[b]	9.4[c]	85.1[c]

[a] Unit = kcal/mol. [b] $\Delta H_f^\circ{}_0(C_2H_4-H_2O)$ and the lowest two frequencies of $C_2H_4-H_2O$ are adjusted to match the experimental results in Figure 5. [c] $\Delta H_f^\circ{}_0$ (C_2H_5OH) = −51.95,[16] $\Delta H_f^\circ{}_0$ (H_2O) = −57.10,[17] $\Delta H_f^\circ{}_0$ (C_2H_4) = 14.58,[17] $\Delta H_f^\circ{}_0$ (CH_3) = 35.86,[18] and $\Delta H_f^\circ{}_0$ (CH_2OH) = −2.75[19] (unit = kcal/mol).

in good agreement with available experimental data for similar reactions,[23] which lie between 1.0×10^{13} and 3.0×10^{13} cm^3 mol^{-1} s^{-1}.

The tunneling effect was considered for reaction R1, because it involves the transfer of a light atom, H.[24] In the present study, the Marcus−Miller quantum approach[25] with a one-dimensional unsymmetrical Eckart potential[26] was employed to account for the hydrogen tunneling effect. The imaginary frequency of $C_2H_4-H_2O$, a parameter in the Eckart function, is nearly the same at the levels of theory considered here (MP2(FC)/6-311G(d,p) and B3LYB/6-31G(d,p)), 1926 and 1928 cm^{-1}, respectively.

The energy increment was fixed at 1 cm^{-1} in all sum and density of states computations. The standard form of the exponential-down model was used for collision energy transfer. In the absence of reliable measurements in the falloff region that are normally used to calibrate the collision model, the model parameters have to be assigned a priori. Specifically, following recommendations of Knyazev et al.[27] on the basis of their extensive comparisons of theoretical predictions with the large body of experimental data, we have accounted for both temperature and energy dependencies of the main collision model parameter, energy transfer per downward collision, $\langle \Delta E_{down} \rangle$, using the following expression:

$$\langle \Delta E_{down} \rangle = ATE^{1/2} \qquad \text{(E2)}$$

where T is the temperature, E is the internal energy, and A is an adjustable constant taken as 3.3×10^{-3} cm$^{-1/2}$ K^{-1} in the present study, which yields approximately 500 cm^{-1} at 1000 K and the energy corresponding to the barrier of reaction R1. The influence of $\langle \Delta E_{down} \rangle$ on the calculated rate constants will be discussed later. The collision frequency of ethanol with the bath gas, nitrogen, was estimated from the Lennard-Jones parameters adopted from ref 28. Because C_2H_5OH is a polar molecule, we have also investigated the influence of the ethanol dipole moment on its collision frequency with the bath gas molecules using the expressions described in ref 28. This effect was found to be unimportant (below 0.6%) over the entire temperature range 300−2500 K. An energy grain size of 10 cm^{-1} was used in the master equation solutions, and the resulting matrix size was 7410 × 7410. This grain size provided numerically

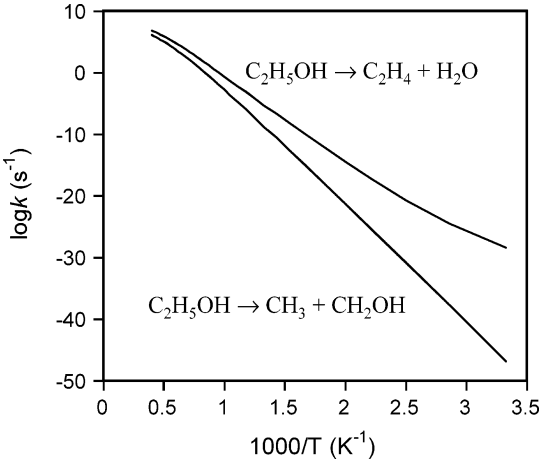

Figure 7. Rate constants of the reactions R1 and R2 at 1 atm.

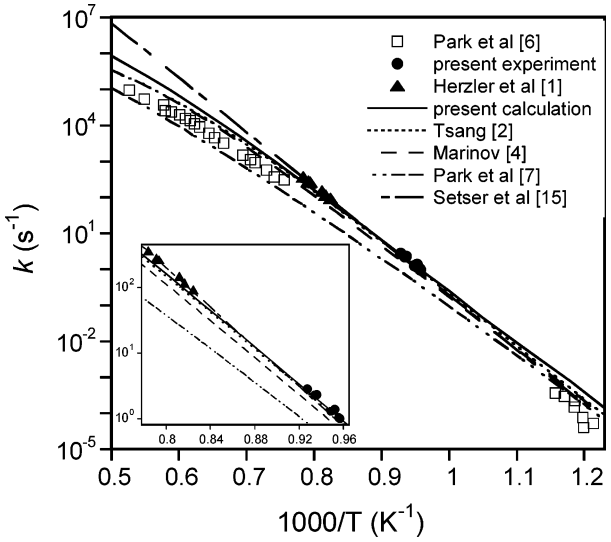

Figure 8. Rate constant of the reaction $C_2H_5OH \rightarrow C_2H_4 + H_2O$. Symbols represent experimental data; lines are theoretical calculation results at 1 atm, except that of Setser et al.[15] which represents the high-pressure-limit rate constant.

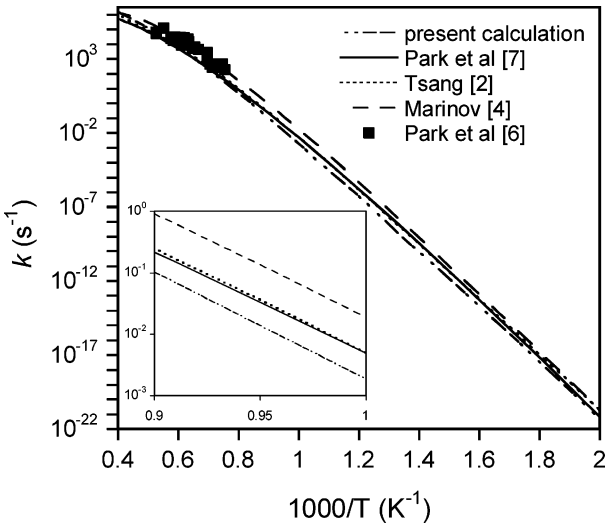

Figure 9. Rate constant of the reaction $C_2H_5OH \rightarrow CH_3 + CH_2OH$ at 1 atm.

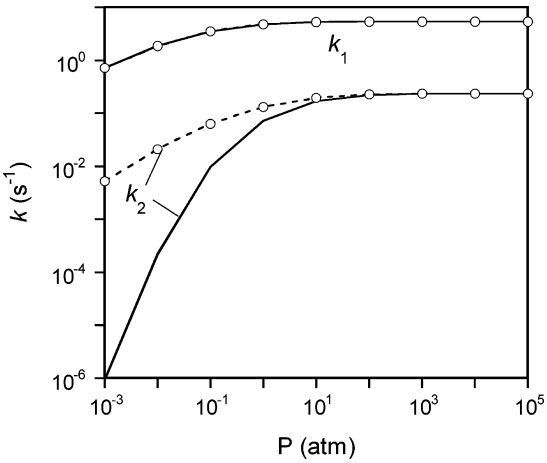

Figure 10. Rate constants of the reactions R1 and R2 at 1100 K. Solid lines: multichannel calculations. Dashed lines with symbols: only the reaction R1 or R2 is considered.

convergent results for all temperatures and pressures considered in this study.

Results and Discussion

The calculated rate constants of reactions R1 and R2 over the temperature range 300−2500 K at 1 atm are presented in Figure 7. The H_2O elimination reaction R1 is observed to be the dominant decomposition channel at 1 atm over the entire temperature range. Figure 8 demonstrates that the calculated k_1 is in excellent agreement with both the shock-tube measurements of Herzler et al.[1] and the theoretical work of Tsang.[2] The result also agrees with that of Marinov[4] within 45%, but is approximately 3.2 times higher than the theoretical value of Park et al.[7] at 1100 K and 1 atm. The present theoretical extrapolation gives values consistently higher than the experimental data reported by Park et al.,[6] with a difference of approximately a factor of 4.5 for the low-temperature (820−860 K) data set and a factor of 3 for the high-temperature data set (Figure 8).

Figure 9 shows that the computed k_2 is approximately 2.4 times lower than that of Tsang[2] at 1100 K and 1 atm. This is caused partly by the choice of $k_{-2\infty}$, which is 3.0×10^{13} cm^3/mol/s in ref 2. If this value for $k_{-2\infty}$ is used, the computed k_2 would agree with the result of Tsang[2] within 8%. The present theoretical value is also approximately a factor of 3.8 times lower than the data reported by Park et al.[6]

The pressure dependencies of rate constants k_1 and k_2 at 1100 K are plotted in Figure 10. The figure also includes the results when the reactions R1 and R2 are treated independently (i.e., ignoring the other channel). The value of k_1 obtained in the multichannel calculation is nearly the same as that of the isolated reaction R1. The values of k_2 obtained in both the multichannel and single-channel calculations approach $k_{2\infty}$ at pressures higher than approximately 100 atm. However, at lower pressures, the value of k_2 in the multichannel calculation is much smaller than that derived from the single-channel calculation, consistent with the conclusion of Tsang.[2] Channel R1 is observed to exhibit the classical falloff shape and reaches the high-pressure limit smoothly with increasing pressure. Channel R2, on the other hand, shows a more complex falloff shape. In the falloff range, k_2 obtained from the multichannel calculation increases much more quickly than that in the single-channel calculation, effectively exhibiting an order of reaction that is higher than 2, and finally reaches the pressure-independent (high-pressure-limiting) asymptote. This shape is a result of the complex evolution of the reactant energy level population in the multichannel systems that can be captured only with the full

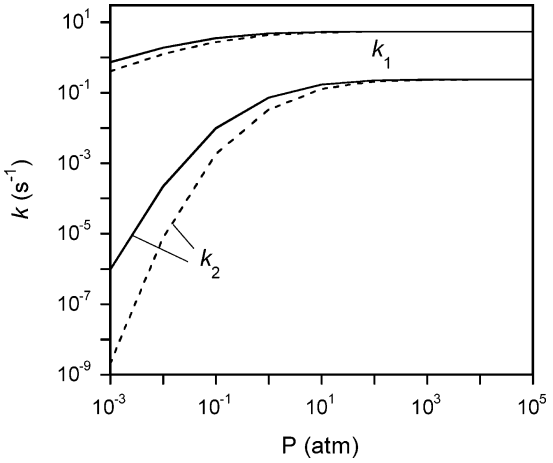

Figure 11. Influence of $\langle \Delta E_{down} \rangle$ on the rate constants of the reactions R1 and R2 at 1100 K. Solid lines: $A = 3.3 \times 10^{-3}$ cm$^{-1/2}$ K^{-1} in the equation (eq E2). Dashed lines: $A = 1.7 \times 10^{-3}$ cm$^{-1/2}$ K^{-1}.

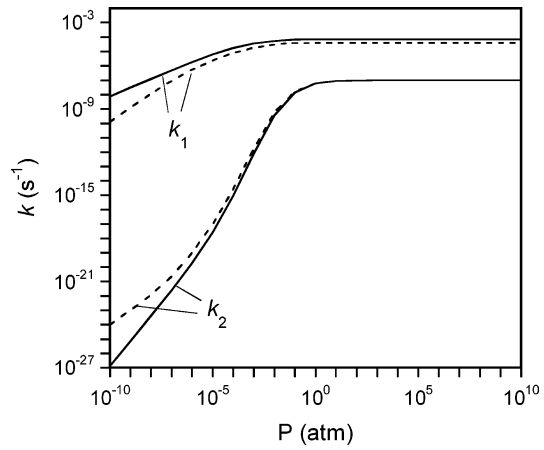

Figure 12. Rate constants of the reactions R1 and R2 at 800 K. Solid lines: with tunneling for R1. Dashed lines: without tunneling for R1.

solution of the master equation and cannot be observed using the modified strong-collision model treatment.[29−30]

In addition to uncertainties yielded from those of $k_{-2\infty}$, the theoretical result is also affected by the choice of $\langle \Delta E_{down} \rangle$. Figure 11 shows the influence of $\langle \Delta E_{down} \rangle$ on the calculated values of k_1 and k_2 at 1100 K with the coefficient A in the equation E2 changing from 3.3×10^{-3} to 1.7×10^{-3} cm$^{-1/2}$ K^{-1} (reduction by a factor of 2). The calculated k_1 is much less sensitive to variation in $\langle \Delta E_{down} \rangle$ than k_2. At low pressures ($\sim 10^{-3}$ atm), k_2 changes by a factor of 2−3 with decreasing $\langle \Delta E_{down} \rangle$. As expected, the influence of $\langle \Delta E_{down} \rangle$ decreases very rapidly with pressure. For example, at 10 atm, k_2 changes only 20% with a doubling of $\langle \Delta E_{down} \rangle$.

Figure 12 illustrates the influence of tunneling on the shape of the falloff range curve by comparing the pressure-dependent behavior of k_1 and k_2 for the cases with and without tunneling. Quantum tunneling has a significant effect on the microscopic rate constant $k_1(E)$, because it effectively lowers the reaction barrier.[24] As a result, tunneling leads to a widening of the falloff range of k_1 toward much lower pressures and a significantly larger low-pressure-limit rate constant than without tunneling. The high-pressure-limit values are approached at the same pressures (0.1 atm for k_1 and 10 atm for k_2) in both cases. In the absence of tunneling, k_1 behaves linearly with pressure P at pressures lower than 10^{-8} atm and reaches the low-pressure limit. In the same pressure range, k_1 is proportional to $P^{0.6}$ and is still in the falloff range when tunneling is considered. Because

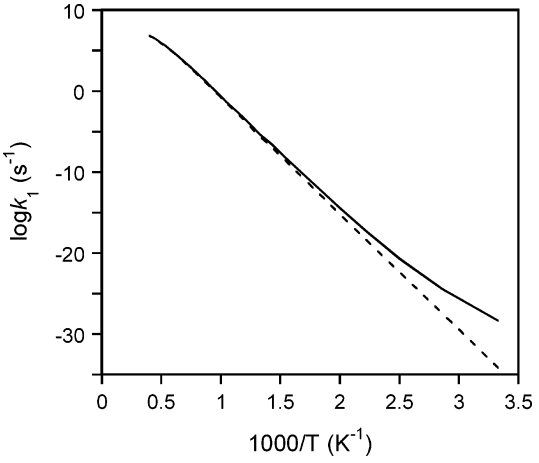

Figure 13. Rate constant of the reaction $C_2H_5OH \rightarrow C_2H_4 + H_2O$ at 1 atm. Solid line: with tunneling. Dashed line: without tunneling.

$k_1(E)$ in the presence of tunneling is cut off at a much lower energy barrier than without tunneling, more reactant molecules are consumed by reaction R1 in the former case. As a consequence of competition with reaction R1 for the reactant molecules, k_2 in the presence of tunneling is much smaller than it is without tunneling, as shown in Figure 12. Because the collisional energy transfer rate increases with pressure, the perturbation to k_2 caused by the change of the $k_1(E)$ function becomes less pronounced at higher pressures.

Figure 13 shows the calculated k_1 at 1 atm with and without tunneling. As expected, the influence of tunneling decreases with temperature. For example, at 500 K, k_1 is approximately 5.9 times higher when tunneling considerations are included, while considering tunneling at 2500 K results in only a very small change (only 8%) in k_1. It is clear, however, that tunneling must be taken into account for this system when interpreting the experimental data obtained at lower temperatures (such as in the static-reactor measurements of Park et al.[6]).

Finally, the results of the present calculations over the temperature range 600−2000 K and at various pressures, including the values at the high-pressure limit, are cast in the modified Arrhenius form in Table 3. The Arrhenius formula was found to reproduce the exact values obtained from the solution of the master equations within 30% for the entire range of conditions.

Conclusion

Ethanol pyrolysis experiments in the presence of two different radical trappers, toluene and 1,3,5-trimethylbenzene, were performed in a variable pressure flow reactor at 1.7−3.0 atm and 1045−1080 K. The radical trapper effectively prohibits significant reactions of ethanol with the reactive radicals (CH_3, H, OH, and so on) that would otherwise result from the decomposition products. As a consequence, approximately 92% of the total C_2H_4 formed under these conditions is predicted to be generated by the H_2O elimination reaction R1. As a result, the rate constant k_1 can be determined directly from the measurements of the ethylene formation rate and ethanol concentration. The experimentally determined rates agree very well with extrapolation of the shock-tube determinations that Herzler et al.[1] have reported recently.

The multichannel unimolecular decomposition of ethanol was also investigated using RRKM/master equation calculations. The energies for stable compounds and transition states were initially evaluated at different levels of theory and adjusted further to

TABLE 3: Recommended Expressions for Rate Constants[a] at Different Pressures

pressure (atm)	$C_2H_5OH \rightarrow C_2H_4 + H_2O$	$C_2H_5OH \rightarrow CH_3 + CH_2OH$
1×10^{-10}	$3.77 \times 10^{43}\, T^{-11.92} \exp(-31\,527/T)$	$6.41 \times 10^{34}\, T^{-9.16} \exp(-64\,751/T)$
0.01	$1.61 \times 10^{45}\, T^{-9.69} \exp(-39\,199/T)$	$5.58 \times 10^{50}\, T^{-11.45} \exp(-49\,616/T)$
0.1	$4.27 \times 10^{36}\, T^{-6.95} \exp(-37\,855/T)$	$2.59 \times 10^{54}\, T^{-11.99} \exp(-50\,576/T)$
1	$8.80 \times 10^{25}\, T^{-3.68} \exp(-35\,627/T)$	$1.26 \times 10^{51}\, T^{-10.59} \exp(-50\,759/T)$
10	$1.41 \times 10^{16}\, T^{-0.74} \exp(-33\,322/T)$	$1.39 \times 10^{42}\, T^{-7.71} \exp(-49\,327/T)$
100	$2.66 \times 10^{9}\, T^{1.25} \exp(-31\,645/T)$	$1.07 \times 10^{32}\, T^{-4.63} \exp(-47\,122/T)$
∞	$1.32 \times 10^{5}\, T^{2.52} \exp(-30\,530/T)$	$9.20 \times 10^{22}\, T^{-1.93} \exp(-44\,890/T)$

[a] Unit = s^{-1}.

match thermochemical and kinetic data available experimentally. The calculated k_1 is in excellent agreement with the recent work of Tsang[2] and is approximately 3.2 times higher than the theoretical value of Park et al.[7] at 1100 K and 1 atm. The calculations also show that the molecular reaction is the dominant decomposition channel at 1 atm over the temperature range 300−2500 K.

The multichannel coupled calculation results were reduced in the Arrhenius form for the relevant range of temperatures and pressures to facilitate computations using popular chemical kinetic numerical codes.

Acknowledgment. This work was supported by the Chemical Sciences, Geosciences and Biosciences Division, Office of Basic Energy Sciences, Office of Science, U.S. Department of Energy under Grant DE-FG02-86ER13503. The authors also thank Mr. Paul Michniewicz and Ms. Yolanda Stein for their assistance in performing the experiments. Helpful discussions with Prof. Vadim D. Knyazev are also greatly appreciated.

Appendix A. Evaluation of Rotational Potentials for Hindered Internal Rotations in C_2H_5OH

The rotational potentials for two internal rotors in the C_2H_5OH molecule used in the present calculations were estimated in two steps. First, the electronic energies were computed at the B3LYP/6-31G(d) level as functions of the corresponding torsion angles, ϕ. All coordinates except for the fixed torsion angle were fully optimized. Next, the extrema (stationary) points identified in the previous step were optimized with respect to all coordinates to find both torsion angles and electronic energies at these conditions at the B3LYP/6-31G(d) level, followed by (stationary) G3B3 energy calculations. Finally, the portions of the B3LYP/6-31G(d) rotational potential between the extrema points were linearly scaled to match the differences between the extrema energy values computed at the G3B3 level. The results for internal rotations around the C−C and C−O bonds are presented in Figures 14 and 15, respectively.

The rotation around the C−C bond has 3-fold symmetry. The present B3LYP/6-31G(d) and G3B3 computations agree very well at the maximum point, and the overall potential is in good agreement with the computations of Sun and Bozzelli[31] who also used B3LYP with a larger, 6-31G(d,p) basis set.

In addition to the starting trans configuration, the rotation around the C−O bond reveals two more gauche rotational conformers at approximately 118° and 242° (0° corresponds to the trans conformer) with the overall potential exhibiting a mirror symmetry at $\phi = 180°$ (Figure 15). Calculations at the B3LYP/6-31G(d) level (in agreement with the calculations of Sun and Bozzelli[31]) also indicate that the gauche conformers are approximately 0.29 kcal/mol more stable than the trans conformer. The present G3B3 calculations, however, suggest the opposite (i.e., that the trans conformer is approximately 0.11 kcal/mol more stable than the gauche conformers). A similar result (0.1 kcal/mol) was reported in the G2 study of Curtiss et al.[32] A more recent detailed study of Weibel et al.[33] presents a series of calculations at different levels of theory and also summarizes the results of prior investigations of the energy difference between the trans and gauche configurations of C_2H_5OH. Weibel et al.[33] concluded that the energy difference between the two configurations is very small (±0.15 kcal/mol), making the conformers essentially degenerate. The present G3B3 calculations are consistent with conclusions of Weibel et al.,[33] and the rotational potential scaled in the manner described here was chosen for further use.

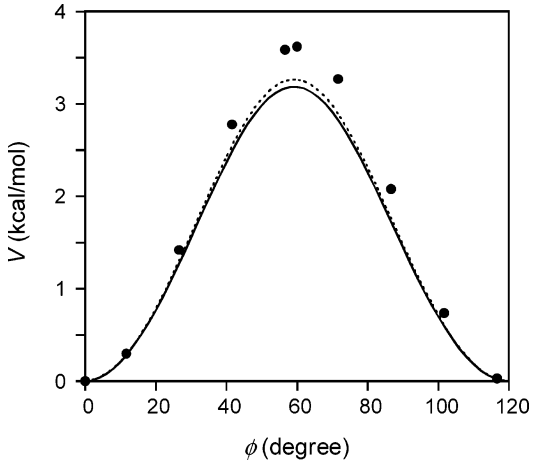

Figure 14. Rotational potential for internal rotation around C−C bond in C_2H_5OH (the portion from 120° to 360° is omitted because of 3-fold symmetry). Symbols: B3LYP/6-31G(d,p) results of Sun and Bozzelli.[31] Dotted line: present B3LYP/6-31G(d) results. Solid line: present B3LYP/6-31G(d) results scaled to match the energy differences between the extema points computed at G3B3 level (see text).

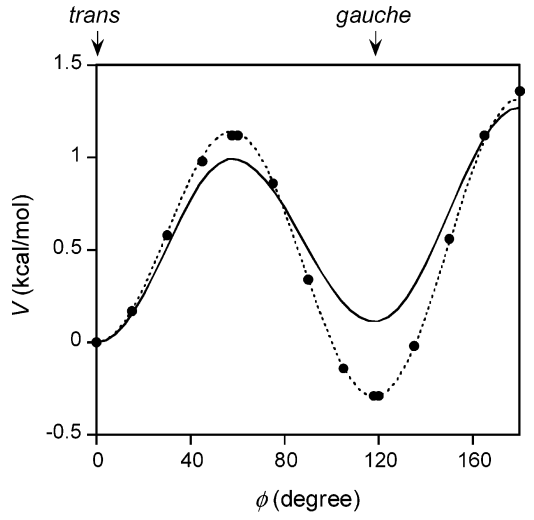

Figure 15. Rotational potential for internal rotation around C−O bond in C_2H_5OH (the portion from 180° to 360° is omitted because of mirror symmetry at the $\phi = 180°$ axis). The symbol and line markings are the same as in Figure 14.

Reduced moments of inertia for C−C and C−O rotors were found to remain nearly constant during the corresponding rotations and were taken at the ground-state configuration obtained at the B3LYP/6-31G(d) level (2.907 and 0.839 amu × Å^2 for C−C and C−O rotations, respectively).

Appendix B. Density of States Inclusive of Hindered Rotations

In the absence of internal hindered rotors, the densities of states needed for evaluation of the RRKM microscopic rate coefficients were computed following the conventional method of Astholz et al.[34] Inclusion of internal hindered rotations into the density of states calculations requires special consideration. Recently, a number of analytical approximations for the density of states of a one-dimensional quantum hindered internal rotor have been proposed.[35,36] These approximations, however, involve two major assumptions: (1) separability of internal rotational degrees of freedom (ignoring the coupling between the external and internal rotational degrees of freedom) and (2) simple sinusoidal (single harmonic) form of rotational potential. Knyazev[36] has concluded that it is assumption 2 that is typically a major source of error in the analytical expressions for the density of states for complex shapes of rotational potentials. Although having an analytical expression certainly presents an advantage, it is possible to evaluate the density of states numerically by using only assumption 1, thus avoiding restriction 2 and substantially increasing the fidelity of the final result. This direct numerical evaluation can also be performed without significant modification of existing numerical algorithms[34] or noticeable computational penalty, as will be discussed next.

To obtain the energy levels, E_n's, of an isolated one-dimensional hindered rotor, one needs to solve the Schrödinger equation:

$$-\frac{\hbar^2}{2I}\frac{\partial^2\psi_n(\phi)}{\partial\phi^2} + V(\phi)\psi_n(\phi) = E_n\psi_n(\phi) \qquad \text{(B1)}$$

where $\hbar$ is the Plank's constant, I is the reduced moment of inertia, ϕ is the torsion angle, $V(\phi)$ is the rotational potential, and $\psi_n(\phi)$ is the wavefunction corresponding to the energy level E_n. The numerical solution of eq B1 for an arbitrary rotational potential can be accomplished by the following actions:[37−40] (1) decomposing the sought wavefunctions $\psi_n(\phi)$'s in the basis of the free-rotor eigenfunction

$$\psi_n^0 = \frac{e^{in\phi}}{\sqrt{2\pi}}$$

and (2) decomposing the rotational potential $V(\phi)$ into a truncated Fourier series

$$V(\phi) = c + \sum_{m=1}^{M}(a_m\cos(m\phi) + b_m\sin(m\phi)) \qquad \text{(B2)}$$

The problem of finding the discrete energy levels, E_n's, is then reduced to the diagonalization of the banded complex Hermitian matrix. The size of the matrix will be defined by N, the number of energy levels to be determined, and the matrix bandwidth is defined by M, the number of Fourier coefficients used to approximate the rotational potential in equation B2. This problem has well-established efficient solution algorithms[41] and does not present any difficulties even for moderately large numbers of levels considered using very modest computational facilities (such as a desktop computer). In the present work, we have developed an in-house computer program which performs the entire task of finding the required number of energy levels given the reduced moment of inertia I and an arbitrary rotational potential defined on a set of discrete points for a ϕ covering the range from 0 to 2π. The number of energy levels determined for C−C and C−O rotors considered in this study was set to 2001, which covered more than an adequate energy range for the density of states calculations. The rotational potentials used in these calculations are described in Appendix A.

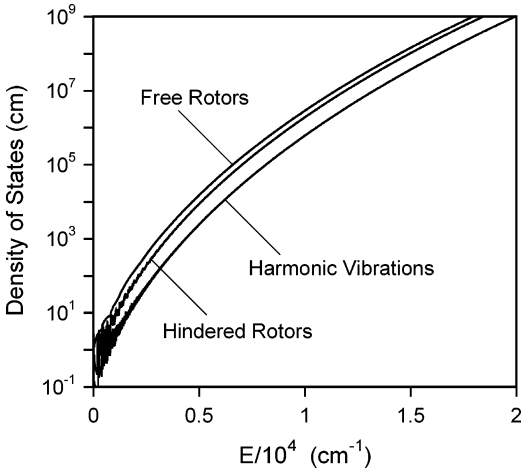

Figure 16. Density of states of C_2H_5OH computed with different treatments of two internal rotations.

Having energy levels E_n's available, the density of states inclusive of internal hindered rotor(s) can be computed via a trivial extension of the method of Astholz et al. In its original implementation,[34] this method involves the initialization of the density of states vector with the analytically evaluated rotational density of states followed by application of the Beyer−Swinehart direct count[42] for harmonic vibrations to the initialized vector. Here, before the application of the Beyer−Swinehart procedure, we fold in the density of states of hindered rotors. This involves the following steps: (1) computing the energy-level vector relative to the zero-point energy (lowest energy level), E_0, of the hinderd rotor, $\epsilon_n = E_n - E_0$ (note that E_0 has to be added to the total zero-point energy of the molecule), and (2) folding in the density of states of the hindered rotor into the current total density of states vector, ρ^{current}

$$\rho(E) = \frac{1}{\sigma}\sum_{n=0}^{N-1}\rho^{\text{current}}(E - \epsilon_n) \qquad \text{(B3)}$$

where σ is the symmetry number of the hindered rotor.

These steps are repeated for each hindered rotor in the system, and the result will incorporate all rotational (free and hindered) degrees of freedom. As in the original method, subsequent application of the Beyer−Swinehart count for harmonic vibrations gives the total density of states.

We note that a direct count via eq B3 was depreciated in the past (for evaluation of the vibrational density of states) for being too computationally expensive. These limitations, however, were due to a relatively large number of vibrational degrees of freedom as well as memory and speed restrictions for early computer systems. The number of hindered rotors is typically much smaller than the number of vibrations, and the modern desktop computer system does not present any restrictions on rapid evaluation of density of states via eq B3 for the values of N of practical interest.

Figure 16 shows the total density of states of C_2H_5OH computed for three different cases. In the first case, the internal

rotations were treated as harmonic vibrations with the corresponding vibrational frequencies taken from the *Gaussian 98* calculations. In the second case, the internal rotors were treated as free rotors. Finally, the third case illustrates a more rigorous hindered rotor approach described above. One can see that more rigorous treatment of internal rotations yields larger values of the density of states as compared to the harmonic oscillator model result previously used for this system.[7,15] This translates to lower values of the microscopic rate constant $k(E)$ and, consequently, lower values of k_∞. One of the major factors responsible for the observed difference is the consideration of two extra gauche states in the treatment of internal rotation around the C−O bond, which are neglected when this degree of freedom is treated as harmonic vibration.

References and Notes

(1) Herzler, J.; Tsang, W.; Manion, J. A. *J. Phys. Chem.* **1997**, *101*, 5500.

(2) Tsang, W. Presented at the 2nd Joint U. S. Sectional Meeting of the Combustion Institute, Oakland, CA, 2001; Paper 92.

(3) *Alternatives to Traditional Transportation Fuels 1996*; DOE/EIA-0585 (96); Energy Information Administration; http://tonto.eia.doc.gov/FTPROOT/alternativefuels/058596.pdf.

(4) Marinov, M. N. *Int. J. Chem. Kinet.* **1999**, *31*, 183.

(5) Li, J.; Kazakov, A.; Dryer, F. L. *Int. J. Chem. Kinet.* **2001**, *33*, 859.

(6) Park, J.; Chen, R.; Chen, J.; Lin, M. C. Presented at Eastern States Section Fall Technical Meeting of the Combustion Institute, Hilton Head, SC, 2001; Paper 187.

(7) Park, J.; Zhu, R. S.; Lin, M. C. *J. Chem. Phys.* **2002**, *117*, 3224.

(8) Emdee, J. L.; Brezinsky, K.; Glassman, I. *J. Phys. Chem.* **1992**, *96*, 2151.

(9) Held, T. J. Ph.D. Thesis, Mechanical and Aerospace Engineering Department, Princeton University, Princeton, NJ, 1993.

(10) Scott, A. P.; Radom, L. *J. Phys. Chem.* **1996**, *100*, 16502.

(11) Curtiss, L. A.; Raghavachari, K.; Trucks, G. W.; Pople, J. A. *J. Chem. Phys.* **1991**, *94*, 7221.

(12) (a) Becke, A. D. *J. Chem. Phys.* **1993**, *98*, 5648. (b) Becke, A. D. *Phys. Rev. A* **1988**, *38*, 3098. (c) Lee, C.; Yang, W.; Parr, R. G. *Phys. Rev. B* **1988**, *37*, 785. (d) Stephens, P. J.; Devlin, F. J.; Chabalowski, C. F.; Frisch, M. J. *J. Phys. Chem.* **1994**, *98*, 11623.

(13) Baboul, A. G.; Curtiss, L. A.; Redfern, P. C.; Raghavachari, K. *J. Chem. Phys.* **1999**, *110*, 7650.

(14) Frisch, M. J.; Trucks, G. W.; Schlegel, H. B.; Scuseria, G. E.; Robb, M. A.; Cheeseman, J. R.; Zakrzewski, V. G.; Montgomery, J. A., Jr.; Stratmann, R. E.; Burant, J. C.; Dapprich, S.; Millam, J. M.; Daniels, A. D.; Kudin, K. N.; Strain, M. C.; Farkas, O.; Tomasi, J.; Barone, V.; Cossi, M.; Cammi, R.; Mennucci, B.; Pomelli, C.; Adamo, C.; Clifford, S.; Ochterski, J.; Petersson, G. A.; Ayala, P. Y.; Cui, Q.; Morokuma, K.; Malick, D. K.; Rabuck, A. D.; Raghavachari, K.; Foresman, J. B.; Cioslowski, J.; Ortiz, J. V.; Stefanov, B. B.; Liu, G.; Liashenko, A.; Piskorz, P.; Komaromi, I.; Gomperts, R.; Martin, R. L.; Fox, D. J.; Keith, T.; Al-Laham, M. A.; Peng, C. Y.; Nanayakkara, A.; Gonzalez, C.; Challacombe, M.; Gill, P. M. W.; Johnson, B. G.; Chen, W.; Wong, M. W.; Andres, J. L.; Head-Gordon, M.; Replogle, E. S.; Pople, J. A. *Gaussian 98*, revision A.1.; Gaussian, Inc.: Pittsburgh, PA, 1998.

(15) Butkovskaya, N. I.; Zhao, Y.; Setser, D. W. *J. Phys. Chem.* **1994**, *98*, 10779.

(16) Frenkel, M.; Chirico, R. D.; Friend, D. G.; Hong, X.; Laesecke, A.; Magee, J. W.; Perkins, R. A. *TRC Thermodynamic Tables, Hydrocarbons*; Thermodynamic Research Center: College Station, TX, 1986.

(17) Chase, M. W., Jr. NIST-JANAF Thermochemical Tables, 4th ed.; *Journal of Physical Chemistry Reference Data*; American Chemical Society: Washington, DC, 1998; Monograph 9.

(18) Ruscic, B.; Litorja, M.; Asher, R. *J. Phys. Chem. A* **1999**, *103*, 8625.

(19) Johnson, R.; Hudgens, J. *J. Phys. Chem.* **1996**, *100*, 19874.

(20) Mokrushin, V.; Bedanov, V.; Tsang, W.; Zachariah, M.; Knyazev, V. *ChemRate*, version 1.19; NIST: Gaithersburg, MD, 2002.

(21) Gilbert, R. G.; Smith, S. C. *Theory of Unimolecular and Recombination Reactions*; Blackwell Scientific Publications: Oxford, U.K., 1990.

(22) Tsang, W. *J. Phys. Chem. Ref. Data* **1987**, *16*, 471.

(23) (a) Du, H.; Hessler, J. P.; Ogren, P. J. *J. Phys. Chem.* **1996**, *100*, 974. (b) Pesa, M.; Pilling, M. J.; Robertson, S. H.; Wardlaw, D. M. *J. Phys. Chem. A* **1998**, *102*, 8526. (c) Forst, W. *J. Phys. Chem.* **1991**, *95*, 3612.

(24) Knyazev, V. D.; Slagle, I. R. *J. Phys. Chem.* **1996**, *100*, 16899.

(25) (a) Marcus, R. A. *J. Chem. Phys.* **1966**, *45*, 2138. (b) Miller, W. H. *J. Am. Chem. Soc.* **1979**, *101*, 6810.

(26) Eckart, C. *Phys. Rev.* **1930**, *35*, 1303.

(27) Knyazev, V. D.; Slagle, I. R. *J. Phys. Chem. A* **2001**, *105*, 3196.

(28) Kee, R. J.; Dixon-Lewis, G.; Warnatz, J.; Coltrin, M. E.; Miller, J. A.; Moffat, H. K. *A FORTRAN Computer Code Package for the Evaluation of Gas-Phase, Multicomponent Transport Properties*; Sandia National Laboratories Report SAND 86-8246B; Sandia: Albuquerque, NM, 1986.

(29) Just, Th.; Troe, J. *J. Phys. Chem.* **1980**, *84*, 3068.

(30) Just, Th. Presented at the 25th Symposium (International) on Combustion; The Combustion Institute, Pittsburgh, PA, 1994; Paper 687.

(31) Sun, H.; Bozzelli, J. W. *J. Phys. Chem. A* **2001**, *105*, 9543.

(32) Curtiss, L. A.; Lucas, D. J.; Pople J. A. *J. Chem. Phys.* **1995**, *102*, 3292.

(33) Weibel, J. D.; Jackels, C. F.; Swofford, R. L. *J. Chem. Phys.* **2002**, *117*, 4245.

(34) Astholz, D. C.; Troe, J.; Wieters, W. *J. Chem. Phys.* **1979**, *70*, 5107.

(35) Witschel, W.; Hartwigsen, C. *Chem. Phys. Lett.* **1997**, *273*, 304.

(36) Knyazev, V. D. *J. Phys. Chem. A* **1998**, *102*, 3916.

(37) Marston, C. C.; Balint-Kuri, G. G. *J. Chem. Phys.* **1989**, *91*, 3571.

(38) Lay, T. H.; Krasnoperov, L. N.; Venanzi, C. A.; Bozzelli, J. W.; Shokhirev, N. V. *J. Phys. Chem.* **1996**, *100*, 8240.

(39) Van Speybroeck, V.; Van Neck, D.; Waroquier, M.; Wauters, S.; Saeys, M.; Marin, G. B. *J. Phys. Chem. A* **2000**, *104*, 10939.

(40) Dimeo, R. M. *DAVE: Data Analysis and Visualization Environment*. NIST: Gaithersburg, MD, http://www.ncnr.nist.gov/dave/documentation/methylcalc.pdf (2002).

(41) Anderson, E.; Bai, Z.; Bischof, C.; Blackford, S.; Demmel, J.; Dongarra, J.; Du Croz, J.; Greenbaum, A.; Hammarling, S.; McKenney, A.; Sorensen, D. *LAPACK Users' Guide*, 3rd ed.; SIAM: Philadelphia, PA, 1999.

(42) Beyer, T.; Swinehart, D. F. Algorithm 448: number of multiply-restricted partitions. *Comm. Assoc. Comput. Machines* **1973**, *16*, 379.